

2 Construction and test of a $1 \times 1 \text{ m}^2$ Micromegas 3 chamber for sampling hadron calorimetry at future 4 lepton colliders

**C. Adloff^a, J-J. Blaising^a, M. Chefdeville^{a*}, A. Dalmaz^a, C. Drancourt^a, R. Gaglione^a,
N. Geffroy^a, D. Girard^a, J. Jacquemier^a, Y. Karyotakis^a, I. Koletsou^a, F. Peltier^a,
J. Samarati^a, S. Tsigaridas^b, G. Tsipolitis^b and G. Vouters^a**

^aLaboratoire d'Annecy-le-Vieux de Physique des Particules, Université de Savoie, CNRS/IN2P3
9 Chemin de Bellevue - BP 110, 74941 Annecy-le-Vieux Cedex, France

^bNTUA, National Technical University of Athens,
Zografou Campus, GR-157, 80 Zografou, Greece

5 E-mail: chefdevi@lapp.in2p3.fr

ABSTRACT: Gaseous sampling hadron calorimeters can be finely segmented and used to record showers with high spatial resolution. This imaging power can be exploited at a future linear collider experiment where the measurement of jets by a Particle Flow method will rely first on the tracking capability of the calorimeters. As a result of the relaxed constrain on energy resolution, a hadron
6 calorimeter equipped with granular gaseous detectors read out by simple threshold electronics is considered. For this application, Micromegas chambers of a few meter square size offer some advantages over traditional gaseous detectors using wires or resistive plates. To test the validity of this concept, a Micromegas prototype of $1 \times 1 \text{ m}^2$ size equipped with 9216 readout pads of $1 \times 1 \text{ cm}^2$ has been built. Its technical and basic operational characteristics are reported.

7 KEYWORDS: Keyword1; Keyword2; Keyword3.

*Corresponding author.

9 **Contents**

10	1. Introduction	2
11	1.1 Particle Flow calorimetry	2
12	1.2 Semi-digital hadron calorimetry	2
13	1.3 The Micromegas detector and calorimeter project	2
14	2. Description of the $1 \times 1 \text{ m}^2$ Micromegas prototype	3
15	2.1 Active sensor units	3
16	2.2 Front-end electronics	3
17	2.3 Mechanical design	4
18	3. Tests prior to chamber assembly	4
19	3.1 Electronics calibration	4
20	3.1.1 Method	4
21	3.1.2 Shaper gains and noise	5
22	3.1.3 Setting of thresholds and pedestals	6
23	3.2 X-ray tests	7
24	3.2.1 Threshold scans	7
25	3.2.2 Mesh voltage scan	8
26	3.2.3 Position scan	9
27	4. Functional tests of the prototype in particle beams	10
28	4.1 Noise conditions in triggered operation	10
29	4.2 Trigger-less operation	11
30	4.3 Response of the six Micromegas meshes	12
31	4.4 Effect of the peaking time	13
32	4.5 Impact of dead zones between ASUs	14
33	4.6 Shower sampling with three readout thresholds	15
34	4.7 Analogue readout of shaper signals	16
35	4.8 Power-pulsing of the front-end chips	17
36	5. Conclusion	17

38 **1. Introduction**

39 **1.1 Particle Flow calorimetry**

40 The detailed study of electroweak symmetry breaking and of the properties of a hypothetical stan-
41 dard model Higgs boson are some of the physics goals motivating the construction of a linear
42 electron collider (ILC [1] or CLIC [2]). This physics case is now enhanced with the discovery at
43 LHC of a Higgs-like new particle [3, 4]. Most of the interesting physics channels at a linear collider
44 will appear in multi-jet final states, often accompanied by charged leptons and missing transverse
45 energy. The di-jet energy resolution should be good enough to identify Z and W bosons in their
46 hadronic decay channels with an accuracy comparable to their natural decay width. This requires
47 an excellent jet energy resolution of 3–4 % over the whole energy range.

48 Two techniques are studied by the DREAM [5] and CALICE [6] collaboration to meet this
49 goal. The first one, called Dual Readout, is a compensation technique that uses cherenkov and
50 scintillation light produced in hadron showers to correct for fluctuations of the electromagnetic
51 fraction which otherwise dominate the jet energy resolution [7]. The Particle Flow technique uses
52 highly segmented calorimeters and a precise tracker to separate the jet’s charged and neutrals com-
53 ponents [8]. After separation, the dominant charged component can be measured more precisely
54 with the tracking system resulting in improved jet energy resolution [9].

55 **1.2 Semi-digital hadron calorimetry**

56 Two hadron calorimeters using steel or tungsten absorbers are developed by the the CALICE col-
57 laboration. The first is instrumented with $3 \times 3 \text{ cm}^2$ scintillating tiles read out by SiPM and 12-bit
58 ADCs [10]. The second uses gaseous detectors with smaller segmentation ($1 \times 1 \text{ cm}^2$) and simpler
59 readout (1-bit or 2-bit [11, 12]). Clearly, the first favours single hadron resolution (higher sampling
60 fraction, analogue readout) while the second targets a high shower separation capability (smaller
61 cells) probably at the expense of resolution (digital readout).

62 A digital hadron calorimeter (1-bit, DHCAL) is expected to have two regimes of operation.
63 A low energy linear regime where the response to the electromagnetic and hadronic shower parts,
64 taken separately, is constant. In this regime, Landau fluctuations are suppressed resulting in im-
65 proved resolution with respect to a perfect analogue readout. A higher energy saturated regime
66 where energy information is lost due to under-counting with the consequence that the resolution
67 degrades with increasing hadron energy [13, 14]. The energy frontier between the two regimes de-
68 pends mainly on the cell size and absorber material. In an SiD-like HCAL geometry with $1 \times 1 \text{ cm}^2$
69 pads and steel absorbers [15], Monte Carlo simulation indicates a frontier between 20–30 GeV.

70 The electromagnetic part of hadron showers results in dense energy deposits and is responsible
71 for the saturation of a DHCAL. A way to account for these deposits in the energy reconstruction
72 is to use additional readout thresholds (2-bit, semi-digital HCAL or SDHCAL). With the right
73 threshold settings and energy reconstruction algorithm, it should be possible to correct for the
74 saturation and improve to some extent the resolution.

75 **1.3 The Micromegas detector and calorimeter project**

76 Micromegas is a Micro Pattern Gas Detector (MPGD) that uses a thin mesh to separate the gas
77 volume into two regions [16]. A low field region where primary electrons are released from the

78 atoms and a high field region where they are drifted to and multiplied by avalanche. Thanks a fast
79 collection of the avalanche ions, Micromegas is free of space charge effects up to very high particle
80 rates and therefore well suited for tracking in high rate environments. This property also makes this
81 detector very appealing for calorimetry because signals are proportional to the energy deposited in
82 the drift region. This is an improvement with respect to wire chamber based gaseous calorimeters
83 which suffered from intrinsic signal saturation from the ion space charge around the wire. Also,
84 ageing effects in Micromegas are minimal because it works in simple gas mixtures (*e.g.* Ar/CO₂)
85 and at relatively low electric fields (~ 40 kV/cm with a multiplication gap of $128 \mu\text{m}$).

86 The Micromegas calorimeter project was initiated in 2006. The first step of the project was the
87 characterisation of small prototypes equipped with standard electronics (external front-end boards
88 and VME ADC modules). Based on the successful results [17], the project moved on to the next
89 phase, namely the integration of the electronics on the detector printed circuit board (PCB) and the
90 scaling up of the detector size.

91 **2. Description of the $1 \times 1 \text{ m}^2$ Micromegas prototype**

92 **2.1 Active sensor units**

93 An Active Sensor Unit (or ASU) is a $32 \times 48 \text{ cm}^2$ PCB (8 layers, 1.2 mm thin) segmented into
94 1536 anode pads of $1 \times 1 \text{ cm}^2$. It is equipped with a Micromegas mesh and 24 front-end chips. The
95 mesh is laminated on the PCB pad plane according to the Bulk process [18]. Packaged chips are
96 soldered to the PCB side opposite to the mesh, together with spark protection diodes, other passive
97 components and flat connectors.

98 The ASU chips are read out with 2 Detector Interface boards (DIF, inter-DIF) which also
99 distribute voltage to the front-end electronics and to the Micromegas mesh. ASU and inter-DIF
100 are connected with flat cables in order to minimise the detector thickness and to allow for some
101 mechanical flexibility between the 2 boards. Thanks to flat connectors on both sides of the ASU,
102 several ASUs can be read out in a row (Figure 1 (left)). This is essential in view of the construction
103 of large area chambers as several ASUs can be chained and read out with only one pair of DIF/inter-
104 DIF boards.

105 **2.2 Front-end electronics**

106 The ILC beam will be pulsed and composed of 1 ms long bunch trains separated by 199 ns. During
107 a train, bunches cross each other every 300 ns and calorimeter signals are digitised automatically
108 and associated to the time of a bunch. Between trains, all information is read out from memory
109 to the back-end electronics meanwhile some front-end circuits are turned off to reduce the heat
110 dissipation inside the calorimeter modules. Key features of the front-end electronics are thus self-
111 triggering with memory, time-stamping and power-pulsing.

112 A dedicated front-end chip called MICROROC has been developed [19]. It belongs to a gen-
113 eration of chips optimised for calorimetry at a future linear collider [20]. The MICROROC is a 64
114 channel chip, with 3 readout thresholds and a power-pulsing capability to reduce its consumption
115 from a nominal value of 3.7 mW at 3.5 V per channel to $100 \mu\text{W}$. Each channel input is protected
116 against spark currents by a diode network followed by a charge preamplifier and 2 shapers of

117 low/high gains and tunable peaking time (75–200 ns). The shaper outputs are connected to three
118 discriminators. When a signal crosses the low threshold, the content of the 64 channel matrix is
119 written to memory with a clock time (so-called event). A total of 127 events can be recorded before
120 filling completely the memory. The later is read out either when it is full (ILC or trigger-less mode)
121 or upon the arrival at the chip of an external trigger signal (testbeam mode or trigger mode).

122 The high gain shaper is connected to the low and medium threshold discriminators and has a
123 dynamic range of 200 fC. The low gain shaper has a linear response up to 500 fC and is connected
124 to the high threshold discriminator. The 3 thresholds are set by 10-bit DACs common to the 64
125 channels. Per channel a 4-bit DAC can be used to shift the pedestal voltage with respect to the
126 common thresholds and minimise their dispersions. A detailed characterisation of the detector
127 can be performed thanks to the calibration test input and a multiplexed shaper output (analogue
128 readout). Calibration of the electronics is discussed in section 3.1 and the analogue readout of
129 Micromegas signals is explained in section 4.7.

130 **2.3 Mechanical design**

131 Mechanical constraints to build an ILC hadron calorimeter are stringent. First of all, the calorimeter
132 will be located inside the solenoid magnet which limits the space between absorbers to 8 mm. Also,
133 to minimise dead zones between modules, the front-end electronics is embedded inside the active
134 layers and only readout boards are foreseen at the ends of the modules. Another challenge is the
135 size of active layers which reaches up to $1 \times 3 \text{ m}^2$ in the SiD design.

136 Modular and scalable to larger sizes, the $1 \times 1 \text{ m}^2$ Micromegas prototype consists of 6 ASUs
137 assembled in a one gas volume (Figure 1). Small spacers are inserted in the 1 mm gap between
138 ASUs and support the cathode cover, defining precisely a drift gap of 3 mm (Figure 2). Plastic
139 frames are closing the chamber sides, leaving openings for 2 gas pipes and flat cables for electronics
140 connections. The chamber is eventually equipped with readout boards (3 pairs of DIF/inter-DIF)
141 and a patch panel for voltage distribution.

142 The total chamber thickness amounts to roughly 9 mm which includes 2 mm for the cathode
143 cover, 3 mm of drift gap and less than 4 mm for PCB and ASICs. With this mechanical design, the
144 fraction of non-instrumented area is less than 2 % of the total area defined by the 6 ASUs. Dead
145 zones are mainly caused by the 1 mm gap between ASUs and the 2 mm wide inactive photoresist
146 strips that support the mesh on the four ASU sides.

147 **3. Tests prior to chamber assembly**

148 **3.1 Electronics calibration**

149 **3.1.1 Method**

150 The calibration enables setting the 3 thresholds by providing the electronic gain (DAC/fC) of the
151 two shapers. It consists in injecting voltage pulses to the test capacitor of each channel and chang-
152 ing the relevant threshold every 100 pulses. For a given pulse height (or test charge), the channel
153 response (0/1) versus threshold is measured and latter differentiated. The gain and noise of the
154 shapers is deduced from the mean μ and root mean squared (RMS) σ of the resulting distribution.
155 Non-linearity of the shaper response are also checked by injecting different test charges: 2.5, 12.5,

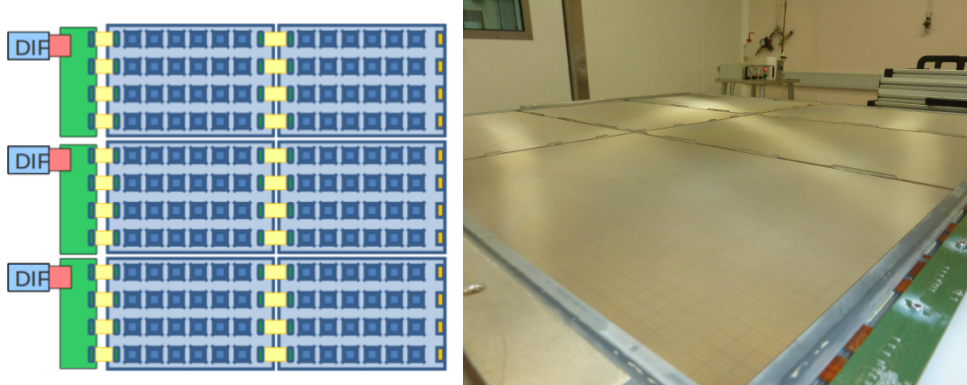


Figure 1. Drawing of the chip side of the $1 \times 1 \text{ m}^2$ prototype showing the readout boards (DIF, inter-DIF), the ASUs and the flexible connectors between them (left). Photograph of the mesh side of the prototype and the drift cover during assembly (right).

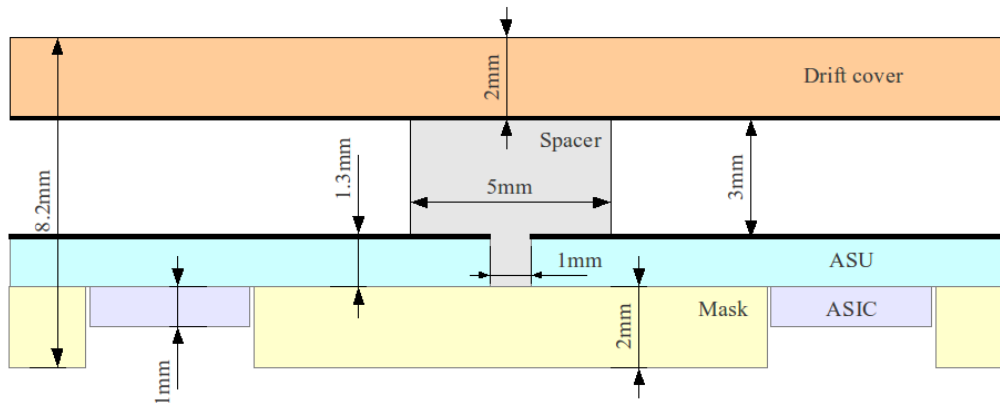


Figure 2. Mechanical design of the $1 \times 1 \text{ m}^2$ prototype at a junction between 2 ASU.

156 22.5 and 32.5 fC for the high gain shaper and 100 and 200 fC for the low gain shaper. The elec-
 157 tronic calibration was performed with a single chip test board after the MICROROC production
 158 and a yield of 91.5 % was found. After bounding of the chips to the PCBs and lamination of the
 159 Bulk mesh, another calibration was performed on the 6 available ASU giving compatible results.
 160 These results are presented in the following section.

161 3.1.2 Shaper gains and noise

162 The gain of the shapers of 9216 channels is distributed around a mean value of 7.0 DAC/fC (high
 163 gain) and 1.6 DAC/fC (low gain). The channel to channel variation in both cases is $\sim 3\%$ RMS
 164 (Figure 3 (left and centre)). This is 3 times smaller than the signal variations induced by mechanical
 165 imperfections of the Micromegas gaps which eventually dominate the response uniformity of this
 166 Micromegas detector [17].

167 The low threshold discriminator triggers the writing to memory of the 64 channel content. It
 168 is connected to the output of the high gain shaper and therefore only the noise of this shaper is
 169 relevant for our purposes. Calculating the noise as σ divided per the gain, an average noise of

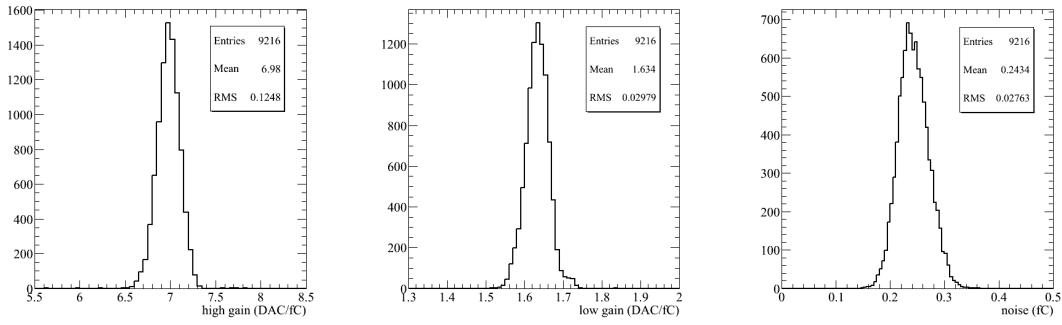


Figure 3. From left to right: gains of the 2 shapers and noise at the output of the high gain shaper for all channels of the $1 \times 1 \text{ m}^2$ prototype.

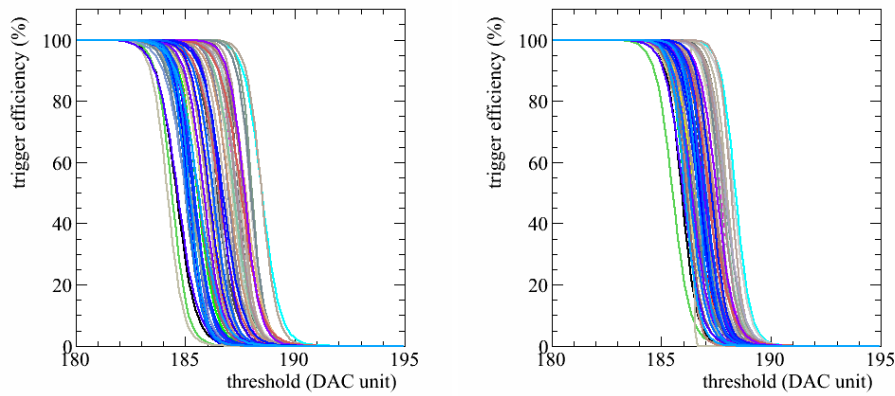


Figure 4. Pedestals of 64 channels measured in a threshold scan before and after alignment (left and right).

170 0.25 fC is found with 10 % variations. This is quite small compared to a typical Micromegas MIP
 171 signal of 5–10 fC and close to what was measured before bounding of the chips to the PCB. It can
 172 thus be concluded that neither the design of the PCB nor the lamination of the mesh increase the
 173 noise level at the channel inputs.

174 3.1.3 Setting of thresholds and pedestals

175 The 3 threshold DACs of a MICROROC are common to the 64 channels. The lowest possible
 176 threshold is therefore determined by the channel of highest pedestal, for instance 5σ above this
 177 pedestal. Also, channels with lower pedestals will experience larger thresholds. As a result, in-
 178 dividual channel DACs have been implemented to change the pedestals and correct the channel
 179 thresholds by a few fC. A method to align the pedestal (and thus to equalise the thresholds) is to
 180 adjust the individual DAC values so as to obtain a uniform noise rate over the all channels. It is
 181 illustrated in Figure 4 and allows to reduce the threshold spread by a factor of 2. This is of sig-
 182 nificant value because a smaller threshold spread allows a lower operating gas gain and low gain
 183 operation is always preferred.

184 In a semi-digital calorimeter, values of the medium and high thresholds should be optimised

185 for best energy resolution over the relevant energy range. This optimisation is meaningful for test
 186 of a full calorimeter, not for single chamber test. During the test beam period reported in section 4,
 187 default settings of 5 and 15 MIPs have been chosen.

188 3.2 X-ray tests

189 Counting experiments are performed with an ^{55}Fe 5.9 keV X-ray source to characterise the ASUs
 190 before they are sealed in the $1 \times 1 \text{ m}^2$ prototype. A dedicated gaseous chamber with 14 mm drift
 191 gap and perforated drift cover has been constructed to measure the response of any of the 1536
 192 ASU channels to true Micromegas signals.

193 In a non flammable mixture of $\text{Ar}/\text{CF}_4/i\text{C}_4\text{H}_{10}$ 95/3/2, ^{55}Fe quanta can convert in the gas
 194 mainly by photoelectric effect on an argon atom, resulting on average in 115 or 230 primary elec-
 195 trons depending on the involved atom relaxation process: fluorescence (escape peak) or Auger
 196 cascade (photopeak) [21]. After drifting, mostly all primary electrons are multiplied in the ampli-
 197 fication gap [17]. If above threshold, the pad signal is recorded as a hit in the chip memory. The
 198 counting rate was measured for various sets of experimental parameters (thresholds, mesh voltage
 199 and pad position). Each run lasted 60 s and the drift field was set to 300 V/cm which corresponds
 200 to the local maximum of the drift velocity in the gas mixture used. Results are presented and
 201 discussed in the following sections.

202 3.2.1 Threshold scans

203 The gas gain curve is deduced from measurements of the counting rate R versus threshold t at var-
 204 ious mesh voltages and using inputs from the electronic calibration (shaper gains). Low threshold
 205 scans were performed at voltages between 300 and 350 V. At a drift field of 300 V/cm, the average
 206 spread of a point-like cloud of electrons (from photoelectric conversion) at the mesh is $\sim 230 \mu\text{m}$
 207 in the direction transverse to the field and $\sim 2 \text{ ns}$ in time [22]. With the source collimated to the
 208 centre of a pad, most primary electrons are collected on one pad. For simplicity all other pads were
 209 electronically disabled. The results are shown in Figure 5. Each $R(t)$ trend is well described by the
 210 sum of two sigmoid functions accounting for the photopeak and the escape peak:

$$R(t) = \frac{p_0}{1 + \exp\left(\frac{t-p_1}{p_2}\right)} + \frac{p_3}{1 + \exp\left(\frac{t-p_4}{p_5}\right)} \quad (3.1)$$

211 where the parameters (p_0, p_3) are the rates at zero threshold, (p_1, p_4) the inflexion thresholds at the
 212 peak maxima and (p_2, p_5) are proportional to the peak widths. In order to reduce the number of
 213 parameters fitted to the data points, the following approximations between photopeak and escape
 214 peak are used:

$$\frac{p_0}{p_3} = \frac{1-f}{f} = \frac{85}{15} \quad (3.2)$$

215 where f is the fluorescence yield of an excited argon atom [23]. Noting E_{pp} and E_{ep} the energy of
 216 the photopeak and escape peak:

$$\frac{p_1}{p_3} = \frac{E_{\text{pp}}}{E_{\text{ep}}} = 2 \quad (3.3)$$

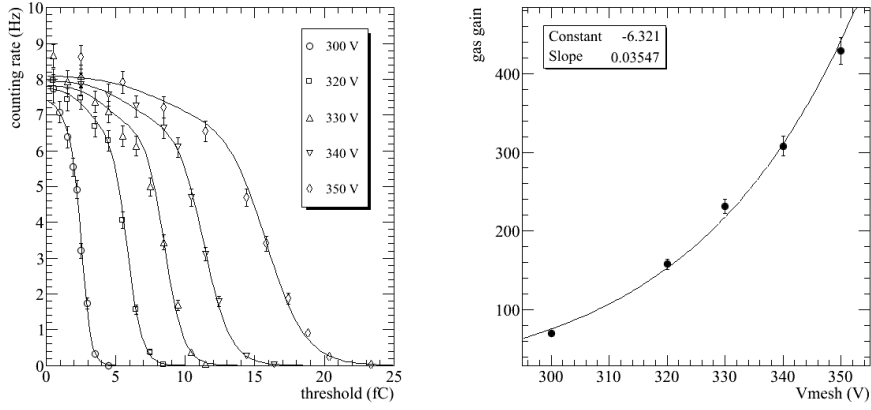


Figure 5. Counting rate versus threshold (left) and resulting gas gain curve (right).

$$\frac{p_2}{p_3} = \sqrt{\frac{E_{pp}}{E_{ep}}} = \sqrt{2} \quad (3.4)$$

217 so Equation 3.1 becomes:

$$R(t) = p_0 \left[\frac{0.85}{1 + \exp\left(\frac{t-p_1}{p_2}\right)} + \frac{0.15}{1 + \exp\left(\frac{t-0.5p_1}{p_2/\sqrt{2}}\right)} \right] \quad (3.5)$$

218 After fitting, all hit rates converge to roughly 8 Hz at zero threshold. Taking an average of 230
 219 primary electrons for photopeak events, the measured charge at the inflexion points (p_1) is used to
 220 calculate the gas gain. The gain exhibits the usual exponential dependence on the mesh voltage
 221 (Figure 5) with a slope of 0.032/V typical of argon-based gas mixtures [24]. At 350 V, a scan of
 222 the high threshold was performed too. The resulting $R(t)$ trend is showed in Figure 6 together with
 223 the low threshold trend. The two threshold scans give gas gain values of 323 and 300 respectively.
 224 The agreement is reasonable and the 4 % difference can probably be explained by systematic errors
 225 during the calibration.

226 3.2.2 Mesh voltage scan

227 The smallest detectable charge can be deduced from a measurement of the counting rate versus gas
 228 gain. In this study, the source is still collimated to the centre of a single pad while the other pads
 229 are disabled. The threshold of the tested pad is set by iteratively decreasing the discriminator DAC
 230 until the count rate becomes dominated by noise. The final DAC value is then set one unit above
 231 this steep transition so this configuration can be defined as the configuration of lowest workable
 232 threshold.

233 The counting rate is measured at various mesh voltages (200–400 V) in this configuration of
 234 lowest threshold. As showed in Figure 6 (right), it increases with voltage as the charge spectrum
 235 shifts above threshold. The trend can be described by an sigmoid function with an inflexion point
 236 at 260 V. At this voltage, the rate is per definition half of its maximum value which implies that the
 237 threshold is equal to the average pad charge. The smallest detectable charge is then given by:

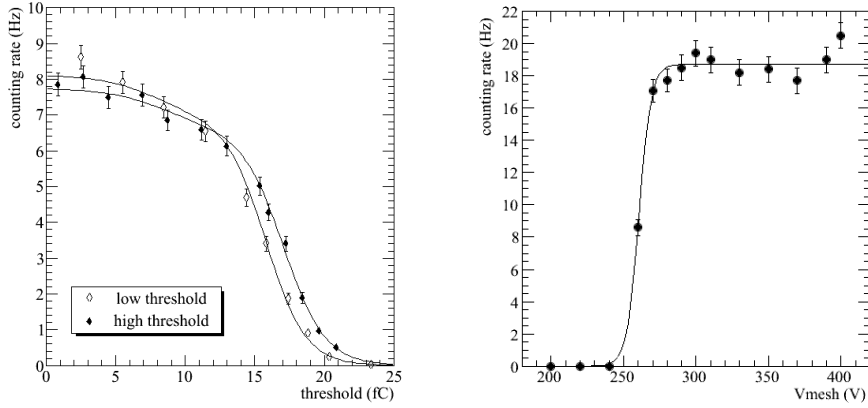


Figure 6. Counting rate versus threshold (left) and mesh voltage (right).

$$Q = q_e N G = 1.6 \cdot 10^{-4} \cdot 212 \cdot 20 \approx 0.7 \text{ fC} \quad (3.6)$$

238 where N is averaged over the ^{55}Fe spectrum (*i.e.* $0.85 \cdot 230 + 0.15 \cdot 115$). Previous measurements
 239 showed that high MIP efficiency ($> 95\%$) is reached when the most probable value of the charge
 240 is ~ 3 times larger than the threshold [17]. Taking a most probable number of primary electrons of
 241 14 (ref X), it can be inferred this condition will be met at gas gains of 1000–2000 only.

242 3.2.3 Position scan

243 The uniformity of the gas gain and of the thresholds can be verified by measuring the X-ray count-
 244 ing rate at various positions and for different ASUs. For a given ASU, the position scan is per-
 245 formed on 6 different positions. At each position the source is collimated onto a region of 2×2
 246 pads centred in between 4 chips (Figure 7 (left)). In this way, it is possible to involve all 24 ASU
 247 chips in the counting experiment. For this study, all channels are enabled and their thresholds are
 248 equalised according to the procedure explained in section 3.1.3. The mesh voltage is set at 320 V
 249 at which an average ^{55}Fe signal of ~ 5 fC is expected. Given the collimation of the source and the
 250 transverse electron diffusion in the gas, the count rate is now to be calculated over an 8×8 pad
 251 region.

252 Position scans have been performed for 6 ASU before assembly in the $1 \times 1 \text{ m}^2$ prototype.
 253 As illustrated in Figure 7 (right), the response of the channels to the source is uniform. A flat
 254 noise-free background from cosmic particles can be seen when plotting the channel occupancy
 255 in a logarithmic scale. The results are summarised in Table 1. For each ASU, the spread of the
 256 counting rate was observed not to exceed 3% RMS. Small ASU to ASU variations of the mean
 257 rate are observed, probably due to change of atmospheric conditions from one test to the next.

258 The conclusion of the ASU tests prior assembly inside the $1 \times 1 \text{ m}^2$ prototype is that the man-
 259 ufacturing technique and the calibration procedure allow to achieve very low detection threshold,
 260 negligible noise and good response uniformity in a reproducible way. After careful characterisation
 261 of 6 ASU, the first $1 \times 1 \text{ m}^2$ Micromegas prototype with MICROROC readout was constructed in

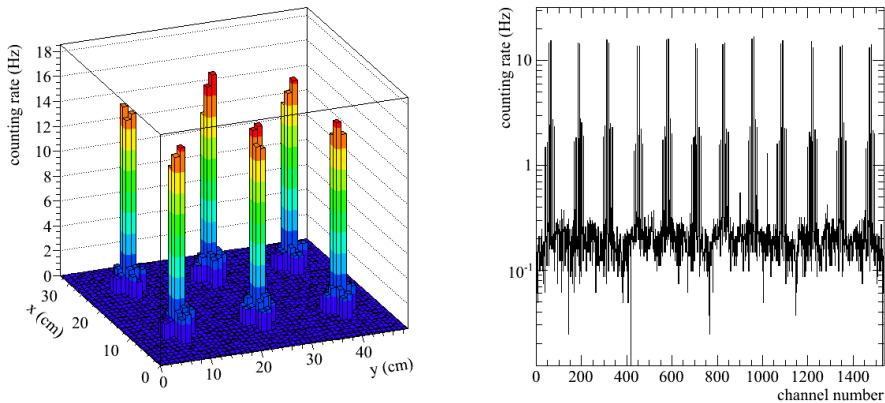


Figure 7. From left to right: two dimensional and one dimensional channel occupancy obtained when moving an ^{55}Fe source over 6 positions.

ASU number	1	2	3	4	5	6
Mean rate (Hz)	86	85	87	79	84	84

Table 1. ^{55}Fe quanta counting rates (± 3 Hz error) measured on 6 ASU (6 measurements per ASU).

262 May 2011 and subsequently tested in beam in July. The results of the test-beam are presented in
 263 the next section.

264 **4. Functional tests of the prototype in particle beams**

265 The goal of the test-beam was to validate the mechanical design of the $1 \times 1 \text{ m}^2$ prototype, to mea-
 266 sure its response to MIPs and to test its principal functionalities. The test set-up consists of the large
 267 prototype and a telescope of small Micromegas chambers and 3 scintillating paddles of $6 \times 16 \text{ cm}^2$
 268 read out by photomultiplier tubes (PMT) (see [17] for a detailed description of the telescope). This
 269 setup-up was installed at the CERN SPS facility in the beam line H4 and exposed to 150 GeV/c
 270 muons and pions. The position of all Micromegas chambers are such that the beam trajectory is
 271 perpendicular to their pad plane. During the pion runs, a 20 cm long block of iron ($10 \times 10 \text{ cm}^2$
 272 cross-section) was placed between the telescope and the prototype to study its behaviour in hadron
 273 showers. The trigger was generated by the time coincidence of the 3 PMT signals and delayed by
 274 $1.5 \mu\text{s}$ before reaching the detectors in order to accommodate for the peaking time of the $1 \times 1 \text{ m}^2$
 275 prototype electronics. To account for the dead time of the telescope and prototype, a gate signal
 276 enters the coincidence such that any PMT signal generating during the readout of the detectors will
 277 be vetoed. The dead time of the whole set-up is dominated by the telescope and is ~ 10 ms.

278 **4.1 Noise conditions in triggered operation**

279 The noise conditions are evaluated by identifying in the $1 \times 1 \text{ m}^2$ prototype data the contributions
 280 from beam muons, cosmic particles and electronic noise. To this end, a low intensity muon beam

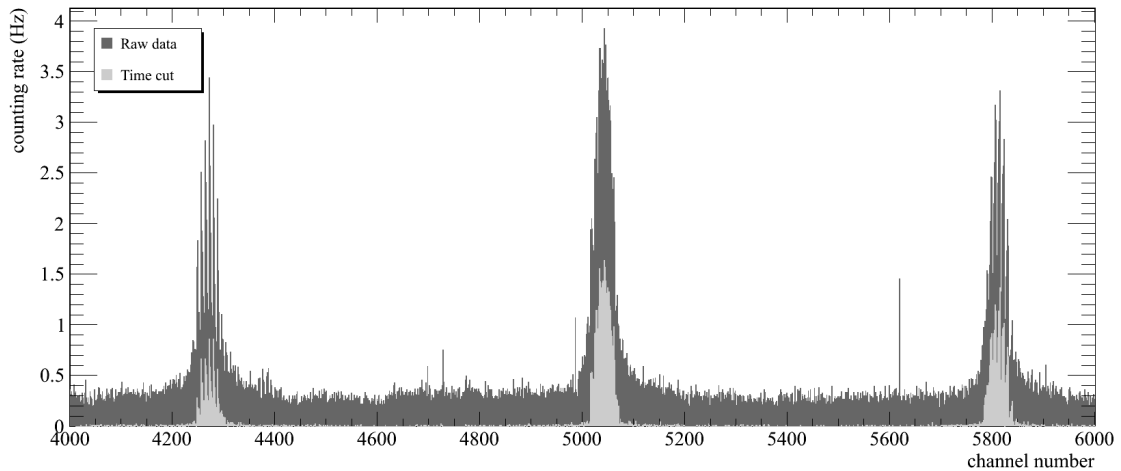


Figure 8. Channel occupancy for all hits and for hits in time with the trigger.

281 of 250 Hz collimated to roughly the size of the scintillators ($\sim 100 \text{ cm}^2$) was used. The mesh
 282 voltage was set to 370 V at which a MIP efficiency larger than 95 % is reached (cf. section 4.4). The
 283 thresholds were equalised according to the procedure previously described, resulting in a number
 284 of disabled channels of 10.

285 The three contributions can be seen in Figure 8 which depicts the counting rate of $\sim 25 \%$ of
 286 the prototype channels. Beam muons appear as broad peaks (the peak shapes are partly the result
 287 of the channel mapping) and a few relatively noisy channels are spotted as isolated peaks. The
 288 background from cosmic particles is essentially flat which demonstrates good noise conditions. By
 289 applying a cut on the time of the trigger ($\Delta t = 1 \mu\text{s}$), cosmic and noise hits are fully suppressed as
 290 illustrated in Figure 8. It can be noted that this cut removes some hits from beam particles as well.
 291 These particles traverse the prototype during a readout. Although vetoed by the trigger, they can
 292 still be recorded by the prototype because its dead time is shorter than the one of the telescope and
 293 because its electronics is self-triggered.

294 **4.2 Trigger-less operation**

295 Thanks to the excellent noise conditions reported in the previous section, the $1 \times 1 \text{ m}^2$ prototype can
 296 actually be operated without an external trigger. In this trigger-less mode, no telescope nor trigger
 297 electronics are used: the prototype is read out when a memory full signal sent by a MICROROC is
 298 received at a DIF board (in trigger mode, a memory full signal resets all chip memory and does not
 299 introduce dead time). The beam and voltage settings of the trigger mode test are used.

300 A simple way to verify that the prototype is efficient in this mode is to compare the average
 301 time between readouts in spill to its expected value. The latter is calculated simply as the ratio
 302 of the memory event depth (127) to the highest chip counting rate ($\sim 130 \text{ Hz}$) and is roughly 1 s.
 303 This is in agreement with measurements as illustrated in Figure 9 (left). Another evidence for an
 304 efficient operation of the prototype in trigger-less mode is showed in Figure 9 (right) where the
 305 channel counting rates in the two modes are compared and found similar. Successful operation

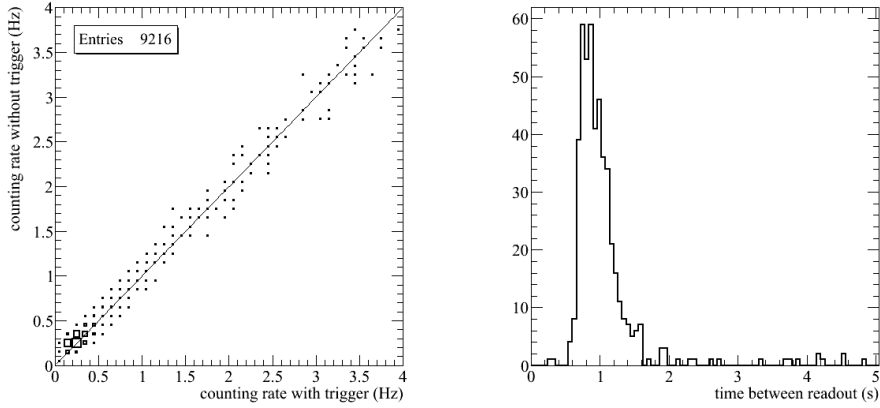


Figure 9. Time between readout in trigger-less mode (left). Channel counting rate during spills (right): trigger versus self-trigger mode.

306 without trigger is possible because of the negligible noise and spark rates which are the result of a
 307 precise electronic calibration and a reliable mesh manufacturing technique.

308 4.3 Response of the six Micromegas meshes

309 The prototype was moved across the beam to measure the MIP efficiency and hit multiplicity of
 310 the 6 ASU. A muon beam of similar intensity as in the previous studies was directed at the centre
 311 of each ASU. At each position, roughly 100 thousand triggers were recorded. Efficiency and hit
 312 multiplicity are deduced from the distribution of the number of hits per triggering muons. This
 313 distribution is built by finding a track in the telescope, extrapolating its impact at the prototype and
 314 counting the number of hits in time with the trigger inside a search region centred around the pad
 315 containing the extrapolated track position. Events are selected by applying the following cuts:

- 316 1. Telescope cut
 317 Single aligned hits in the 3 chambers to select tracks with minimum angle w.r.t. the beam
 318 axis and to extrapolate the track position at the prototype in the most precise way. This cut
 319 reduces the statistics by roughly one third.
- 320 2. Prototype cut
 321 No hits in time with the trigger outside the search region to reduce the impact of multiple
 322 scattering on the measured efficiency. The radial distribution of hits (in time with the trig-
 323 ger) w.r.t. the extrapolated pad falls rapidly and has a long tail from muons scattered in the
 324 last telescope chamber. As a result, a search region of 7×7 pads is chosen. This cut reduces
 325 further the statistics by 5%.

326 About 30 thousand events pass the selection for each ASU. They are used to build the distribution
 327 of the number of hits above the 3 threshold. The efficiency ε of a given threshold is calculated as
 328 the probability to have at least one hit in the search region:

$$\varepsilon = 1 - N_0 / N_t \quad (4.1)$$

329 and the hit multiplicity m as the average number of hits in the search region provided there is at
 330 least one hit in the search region:

$$m = \sum_{i=1}^{21} i \frac{N_i}{N_t - N_0} \quad (4.2)$$

331 where N_i is the number of events with “ i ” hits and N_t the total number of events. Efficiency and
 332 hit multiplicity have been calculated for the 6 ASU and for the 3 thresholds. For the low threshold,
 333 high efficiency and low multiplicity are observed, with little spread from ASU to ASU (Table 2).
 334 As expected, smaller values are observed for the medium and high thresholds. Because these two
 335 thresholds are set within the signal distribution, their response is more sensitive to detector non-
 336 uniformity than the one of the low threshold and indeed, more spread is observed. These variations
 337 could be due to small difference of the amplification gap size from one ASU to the other. They are,
 338 however, not too large and could be attenuated by adjusting the mesh voltage or the corresponding
 339 chip thresholds. In section 4.7, a way to calculate these corrections using the direct readout of
 340 shaper signals is presented.

ASU number	1	2	3	4	5	6
ϵ_0 (%)	97.7	97.5	98.7	98.2	98.2	96.6
m_0 (%)	1.064	1.072	1.079	1.080	1.075	1.079
ϵ_1 (%)	34.8	36.7	46.4	41.0	38.6	46.0
m_1 (%)	1.033	1.033	1.035	1.035	1.037	1.033
ϵ_2 (%)	3.7	3.7	4.6	4.0	4.0	4.6
m_2 (%)	1.050	1.057	1.059	1.075	1.052	1.046

Table 2. MIP efficiency and hit multiplicity of the 6 ASU for the 3 thresholds.

341 4.4 Effect of the peaking time

342 The MICROROC chip was designed for various MPGD geometries, for instance with a Bulk mesh
 343 of different gap size or even with a Gas Electron Multiplier structure. For this purpose, the peaking
 344 time of the preamplifier can be set to 75, 115, 150 or 200 ns (the latter being the default value of the
 345 $1 \times 1 \text{ m}^2$ prototype). In the gas mixture used, the signal from the multiplication of a single primary
 346 electron in a $128 \mu\text{m}$ gap consists of a fast electron peak ($\sim 1 \text{ ns}$) and a long ion tail ($\sim 100\text{--}200 \text{ ns}$).
 347 For a traversing MIP, the signal is the sum of, on average, 30 primary electrons arriving at the mesh
 348 in about 30 ns. Therefore, a strong dependence of the efficiency on the peaking time is expected
 349 and has been measured.

350 This dependence was measured by performing voltage scan for the 4 different values of the
 351 peaking time in a muon beam directed at the centre of one ASU. The efficiency is calculated as
 352 explained in the previous section. The 150 ns and 200 ns trends showed in Figure 10 are similar,

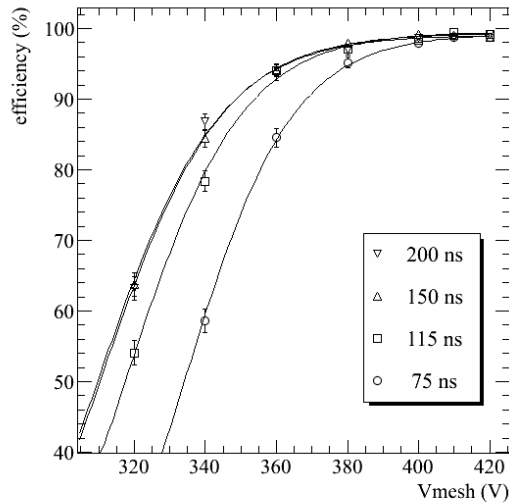


Figure 10. MIP efficiency versus mesh voltage for various peaking time of the MICROROC.

353 meaning that the Micromegas MIP signal is completed in 150 ns or less. The loss of efficiency
 354 from 150 ns to 115 ns peaking time indicates, however, that the signal lasts longer than 115 ns
 355 which is compatible with expectations. At shorter peaking times, an efficiency larger than 95 %
 356 can be maintained by increasing the gas gain. This is illustrated in Table 3 where the voltages for
 357 95 % efficiency are summarised: the loss of signal when changing the peaking time from 200 ns to
 358 75 ns is compensated by a 20 V increase of mesh voltage. These voltages are calculated using the
 359 empirical parametrisation:

$$\varepsilon(V) = \frac{p_0}{1 + \exp\left(\frac{p_1 - V}{p_2}\right)} \quad (4.3)$$

360 where p_0 is the efficiency at infinite voltage, p_1 is the voltage for 50 % efficiency and p_2 describes
 361 the rise of the $\varepsilon(V)$ trend. All adjusted p_0 parameters are compatible and yield an average of
 362 99.3 ± 0.3 %. The fact that this asymptotic value is not equal to 1 could be explained by the dead
 363 zone from the mesh supporting pillars. The voltage p_1 decreases at longer peaking time as a result
 364 of the increased available signal and becomes constant between 115–150 ns. At decreasing peaking
 365 times below 115 ns, the efficiency rises faster with voltages which is accounted for by smaller p_2
 366 values.

367 4.5 Impact of dead zones between ASUs

368 Non-instrumented areas inside the prototype amount to 1.5 % of the total area occupied by the 6
 369 ASUs (96.5×97 cm²). Another contribution to the prototype inefficiency may come from possible
 370 non-uniformity of the electric field at the ASU edges. This hypothesis was tested by placing a
 371 block of iron along a pion beam (collimated to a 3×3 cm² region) and measuring downstream
 372 of the block secondary particles produced in hadron showers. In this way a large fraction of the

t_p (ns)	75	115	150	200
p_0 (%)	99.3 ± 0.3	99.6 ± 0.3	99.4 ± 0.3	99.1 ± 0.3
p_1 (V)	333.9 ± 0.7	317.4 ± 0.8	310.1 ± 0.9	309.4 ± 0.8
p_2 (V)	15.2 ± 0.5	16.3 ± 0.7	17.0 ± 0.8	17.1 ± 0.7
$V(\epsilon = 95\%)$ (V)	380.9	366.7	362.6	363.0

Table 3. Parameters describing the voltage dependence of the efficiency for various peaking time of the MICROROC. The voltage necessary to reach an efficiency of 95 % is indicated in the last line.

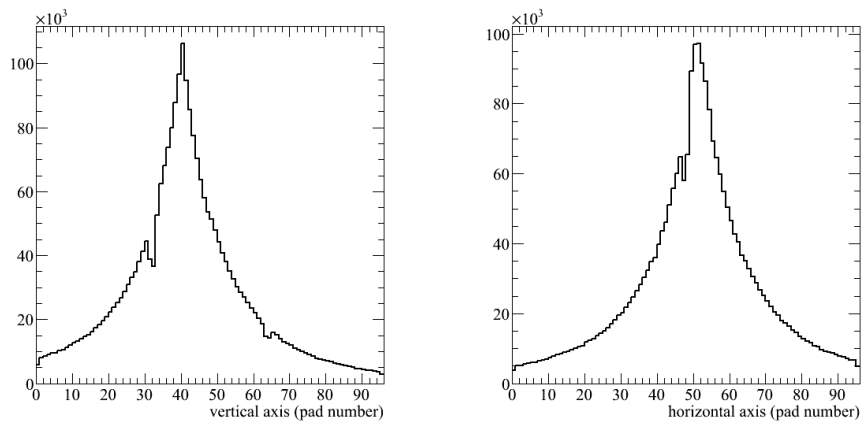


Figure 11. Vertical and horizontal profiles of pion showers (~ 50 thousand events).

373 prototype is exposed and possible discontinuities in the measured hit profile can be looked for. For
374 this measurement, the mesh voltages were set to 375 V.

375 Considering the block size ($10 \times 10 \text{ cm}^2$ transverse size and 20 cm length along the beam),
376 roughly half of the pions experience a nuclear interaction inside the block. The distribution of the
377 number of hits in the prototype thus shows a peak at $N_t = 1$ from penetrating pions and a long tail up
378 to $N_t = 300$ from showering pions. Horizontal and vertical profiles of showers only are constructed
379 by rejecting events with a hit multiplicity below 3. They are showed in Figure 11 where a small drop
380 of efficiency for pads at the ASU edges is observed. By extrapolation of the inner pad occupancy
381 to the ASU edges, the number of hits is 20 % lower than what it should be. The number of pads
382 at the ASU edges is 576 (out of 9216 which yields a fraction of 6.2 %). This can be interpreted as
383 a dead zone of 1.25 % which adds to the 1.5 % from non-instrumented areas, leading to less than
384 3 % of the prototype being inefficient.

385 4.6 Shower sampling with three readout thresholds

386 Hadron showers develop on average into a dense electromagnetic core from neutral meson decays
387 surrounded by a halo of particles (muons, charged pions, protons etc...). Saturation in a DHCAL
388 will be caused mainly by the electromagnetic part and additional thresholds are introduced to per-

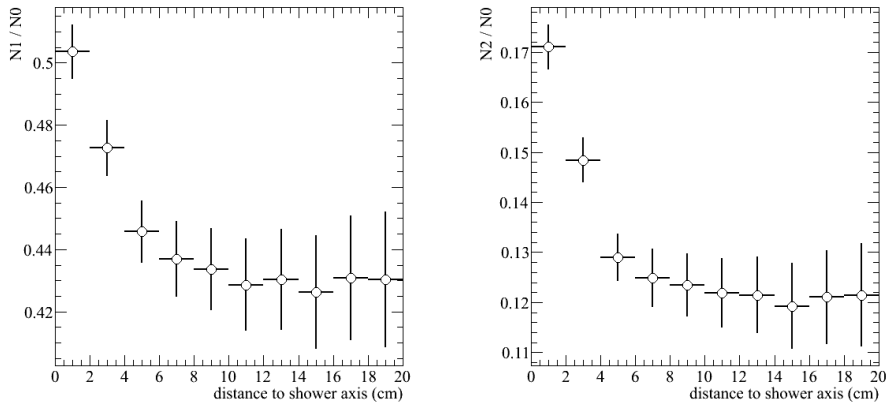


Figure 12. Medium and high threshold efficiency in hadron showers versus distance to the shower axis.

389 haps mitigate this effect by identification and weighting of low, medium and high energy deposits.
 390 This identification capability can be illustrated by measuring the threshold efficiencies for various
 391 energy deposits. Because the energy density decreases with the distance to the shower axis, the
 392 efficiencies were measured as a function of position using the setup-up described in the previous
 393 section. The mesh voltage was 370 V and the thresholds were set at roughly (2 fC, 2 MIP, 10 MIP).

394 Because the MIP efficiency of the low threshold is high ($\leq 95\%$), the efficiency of the other
 395 thresholds can be approximated to N_1/N_0 and N_2/N_0 where N_k is the number of hits from thresh-
 396 old "k". These ratios are plotted versus distance to the shower axis in Figure 12. Both trends
 397 indicate that the electromagnetic core is contained in a circle of 10 cm radius. Compared to the
 398 halo, the core has a higher energy density which explains the probability variation with distance:
 399 N_1/N_0 increases from 0.43 to 0.51 and N_2/N_0 from 0.12 to 0.17. This measurement illustrates the
 400 possibility to identify the electromagnetic part of hadron showers which is a necessary condition
 401 for offline compensation of a Micromegas semi-digital hadron calorimeter.

402 4.7 Analogue readout of shaper signals

403 Correction of the mesh voltage or of the readout threshold may be necessary to improve the re-
 404 sponse uniformity of the prototype, in particular for the medium and high thresholds (cf. section
 405 4.3). The most straight-forward way to calculate the correction is to have access directly to the
 406 signal distribution. For this reason, dedicated lines were implemented on the ASU to read out the
 407 output voltage of the low gain shaper. The analogue readout uses a trigger signal that first arrives
 408 at the DIF. After a certain programmable delay to match the peaking time of the MICROROC, the
 409 DIF forwards the signal at the chips. The voltages of the shaper outputs of all channels are then
 410 multiplexed and sent to the DIF where they are digitised with a 12-bit resolution.

411 The analogue readout was tested in a beam of muons. The Landau distribution as measured
 412 on roughly 100 pads and corrected for channel to channel pedestal variations is shown in Figure 13
 413 (left). By applying cuts on low, medium or high thresholds, the signal distribution is cropped from
 414 0 to the threshold value which can thus be measured in unit of charge (Figure 13 (left to right)).
 415 More importantly, it is also possible to measure the thresholds in unit of the MIP value which is the

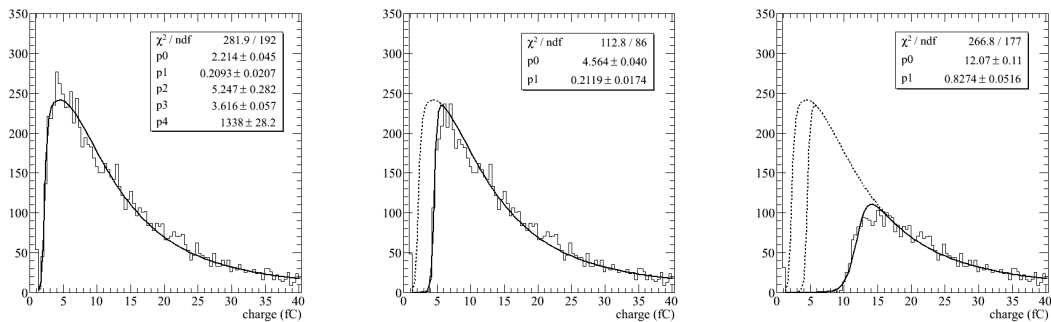


Figure 13. Muon Landau distribution from low, medium and high threshold hits.

416 natural energy unit in a calorimeter. For instance, threshold and MIP values can be extracted from
 417 the data using the following parametrisation of the charge spectrum:

$$f(q) = s(q, p_0, p_1) \cdot l(q, p_2, p_3, p_4) \quad (4.4)$$

418 where $s(q)$ is a sigmoid function of inflexion point p_0 , width p_1 and with a maximum value of 1 that
 419 accounts for the channel to channel threshold dispersion. The function $l(q)$ is the Landau function
 420 of most probable value p_3 , width p_4 and normalisation factor p_2 . When adjusting the parameters to
 421 the data of Figure 13, it is found that (for this particular run) low, medium and high thresholds are
 422 respectively equal to 0.6, 1.3 and 3.3 times the MIP value.

423 4.8 Power-pulsing of the front-end chips

424 The circuits of a MICROROC chip can be turned on and off rapidly according to an external digital
 425 signal (*e.g.* the accelerator clock). When the chip is turned on, a certain programmable delay is
 426 applied before any detector signal can be recorded to the memory. This delay accounts for the
 427 stabilisation of the various voltages and currents inside the chip and should be minimum to reduce
 428 the power consumption. If the delay is too short, the detector occupancy is dominated by noise
 429 until stabilisation. This is illustrated in Figure 14 (left) where the number of hits in the $1 \times 1 \text{ m}^2$
 430 prototype is plotted versus time for a short run in trigger-less mode. During the run, a power-
 431 pulsing timing of 4.5 s off and 3 s on was used and the delay was set to $50 \mu\text{s}$. When using a delay
 432 of $100 \mu\text{s}$ (Figure 14 (right)), the high peaks every 7.5 s disappear because stabilisation has been
 433 achieved. For a bias voltage of 5 V, the current drops from 11 A to 3 A when the chips are turned
 434 off. The 3 A correspond to the consumption of the 3 DIF and inter-DIF boards of the prototype.

435 5. Conclusion

436 A Micromegas prototype of $1 \times 1 \text{ m}^2$ consisting of six independent Micromegas boards with inte-
 437 grated 2-bit front-end electronics has been constructed. This modular design, although introducing
 438 little dead zones (below 3%), allows to achieve an overall thickness of 9 mm and a uniform drift
 439 gap over the prototype area. Thanks to adequate discharge protections and low noise front-end
 440 circuits, more than 99.98 % of the 9216 prototype channels are operational. Most importantly, the

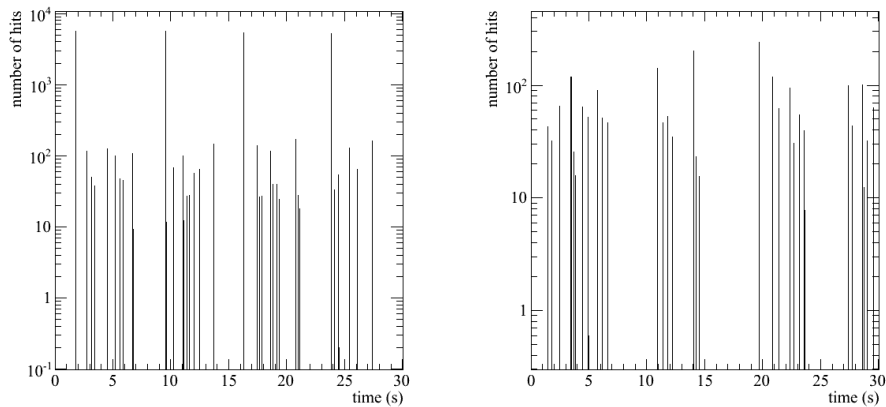


Figure 14. Number of hits versus time using power-pulsing of the chips with $50 \mu\text{s}$ (left) and $100 \mu\text{s}$ (right) delay between the power signal and the start of the trigger-less acquisition.

441 six Micromegas boards exhibit comparable performance to ionising radiations and all provide the
 442 necessary gas gain for a 98 % efficiency to minimum ionising particles.

443 Compared to a pure digital gaseous calorimetry, an approach with three threshold will rely
 444 strongly on the proportionality of the sampling detector and on its cell to cell signal uniformity.
 445 This kind of Micromegas is free of saturation effects and its amplification gap is precisely defined
 446 by the mesh supporting pillars over the anode plane. Variations of this gap have probably been
 447 observed from mesh to mesh. Based on the direct readout of detector signals, however, a technique
 448 to correct the mesh voltage of chip thresholds is possible. Combined with other features such
 449 as power-pulsing and self-triggering, the constructed Micromegas prototype is therefore a good
 450 candidate for Particle Flow calorimetry at a future linear collider.

451 References

- 452 [1] A. Djouadi et al., *International Linear Collider Reference Design Report Volume 2: PHYSICS AT THE*
 453 *ILC*, *arXiv:hep-ph 0709.1893* (2007).
- 454 [2] CLIC Physics Working Group, *Physics at the CLIC Multi-TeV Linear Collider*, *arXiv:hep-ph 0412251*
 455 (2004).
- 456 [3] ATLAS collaboration, *Observation of a new particle in the search for the Standard Model Higgs boson*
 457 *with the ATLAS detector at the LHC*, *Physics Letters B 716* (2012) 1.
- 458 [4] CMS collaboration, *Observation of a new boson at a mass of 125 GeV with the CMS experiment at the*
 459 *LHC*, *Physics Letters B 716* (2012) 30.
- 460 [5] *The RD52 experiment*, <http://highenergy.phys.ttu.edu/dream..>
- 461 [6] *The CALICE collaboration*, <https://twiki.cern.ch/twiki/bin/view/CALICE>.
- 462 [7] R. Wigmans, *The DREAM project-Results and plans*, *Nucl. Instr. and Meth. A 572* (2007) 215.
- 463 [8] J.-C. Brient, H. Videau, *The calorimetry at a future e^+e^- linear collider*, *arXiv:hep-ex 0202004v1*
 464 (2002).

- 465 [9] M.A. Thomson, *Particle flow calorimetry and the PandoraPFA algorithm*, *Nucl. Instr. and Meth. A* **611**
466 (2009) 25.
- 467 [10] V. Andreev et al., *A high-granularity scintillator calorimeter readout with silicon photomultipliers*,
468 *Nucl. Instr. and Meth. A* **540** (2005) 368.
- 469 [11] B. Bilki et al., *Calibration of a digital hadron calorimeter with muons*, *JINST* **3** (2008) 05001.
- 470 [12] S. Mannai et al., *High granularity Semi-Digital Hadronic Calorimeter using GRPCs*, *Nucl. Instr. and*
471 *Meth. A, Article in Press* (2012).
- 472 [13] A. Ghezzi, T. Tabarelli de Fatis, G. Tinti, *Digital Hadron Calorimetry with Glass RPC Active*
473 *Detectors*, *arXiv:physics* **0507021** (2005).
- 474 [14] C. Adloff et al., *Monte Carlo study of the physics performance of a digital hadronic calorimeter*,
475 *JINST* **4** (2009) 11009.
- 476 [15] *SiD Letter of Intent*, *arXiv/physics.ins-det* **0911.0006** (2009).
- 477 [16] Y. Giomataris et al., *MICROMEGAS: a high-granularity position-sensitive gaseous detector for high*
478 *particle-flux environments*, *Nucl. Instr. and Meth. A* **376** (1996) 29.
- 479 [17] C. Adloff et al., *MICROMEGAS chambers for hadronic calorimetry at a future linear collider*, *JINST*
480 **4** (2009) 11023.
- 481 [18] I. Giomataris et al., *Micromegas in a bulk*, *Nucl. Instr. and Meth. A* **vol** (year) page.
- 482 [19] C. Adloff et al., *MICROROC: MICRO-mesh gaseous structure Read-Out Chip*, *JINST* **7** (2012) 01029.
- 483 [20] *Omega, microelectronics for physics and medical imaging*: <http://omega.in2p3.fr/>.
- 484 [21] M. Chefdeville, *Development of Micromegas-like gaseous detectors using a pixel readout chip as*
485 *collecting anode*, *CERN Document Server PhD Thesis* (2009) 151.
- 486 [22] S.F. Biagi, *Monte Carlo simulation of electron drift and diffusion in counting gases under the*
487 *influence of electric and magnetic fields*, *Nucl. Instr. and Meth. A* **421** (1999) 234.
- 488 [23] F. Sauli, *Principles of operation of Multiwire Proportional and Drift Chambers*, *CERN Yellow*
489 *Reports* **77-09** (1977).
- 490 [24] J. Bouchez et al., *Bulk micromegas detectors for large TPC applications*, *Nucl. Instr. and Meth. A* **547**
491 (2007) 425.